Ultrafast Science
A SCIENCE PARTNER JOURNAL

RESEARCH ARTICLE

Control of Valley Polarization Based on Quantum Path Interference

Ling-Jie Lü[1,2] and Xue-Bin Bian[1*]

[1]Wuhan Institute of Physics and Mathematics, Innovation Academy for Precision Measurement Science and Technology, Chinese Academy of Sciences, Wuhan 430071, China. [2]College of Mechanical Engineering, Jiaxing University, Jiaxing 314001, China.

*Address correspondence to: xuebin.bian@wipm.ac.cn

Citation: Lü LJ, Bian XB. Control of Valley Polarization Based on Quantum Path Interference. *Ultrafast Sci.* 2024;4:Article 0078. https://doi.org/10.34133/ultrafastscience.0078

Submitted 2 April 2024
Revised 6 September 2024
Accepted 25 September 2024
Published 13 December 2024

Valleytronic devices based on all-optical ultrafast control are expected to increase the speed of information processing to petahertz and serve a new generation of quantum computers. However, the current difficulty in realizing this vision is the lack of a nondamaging means suitable for ultrafast lasers. We propose a robust scheme to control the valley polarization of monolayer materials, achieved through the quantum interference between 1- and 2-photon transition pathways. The scheme reveals that conventional circularly polarized light is unnecessary for resonantly induced valley polarization and, instead, only a parallel-polarized 2-color field is required. The interference dynamics enables the switch of valley to be manipulated within few femtoseconds without the necessity for extremely strong or single-cycle pulses. The disclosure of this interference scheme enables repetitive operations in valley devices for signal processing at petahertz clock rates without causing material damage. It sheds light on the practical manufacture of high-speed valleytronic devices.

Introduction

Traditional electron circuits are running at gigahertz rates. The advancements in laser-controlled ultrafast electron dynamics opened up new avenues for fundamental research in devices operating at petahertz rates [1,2]. Ludwig et al. [3] induced ultrafast tunnel currents in plasmonic nanocircuits using a single-cycle laser. Despite its reliance on the extremely precise design of lasers and nanostructures, this approach ignited enthusiasm for research into ultrafast switches. Electrons possess an additional degree of freedom aside from charge and spin in certain crystals, known as the valley degree of freedom. The lifetime of valley polarization is 1 to 10^3 ps, which poses challenges for ultrafast valley control [4]. The ability to control and probe valley using ultrafast lasers in recent years suggests that all-optical valley devices hold the promise of surpassing the limitations of traditional electronics and operating at clock rates matching visible light frequencies [5].

The pioneering research [6,7] demonstrated the feasibility of resonant valley polarization employing circularly polarized laser. The subsequent numerical simulations [8,9] indicated that when temporally separating the 2 orthogonal components of a resonant circularly polarized laser, their combination, despite being nonoverlapping, still retained the capacity to induce valley polarization. This resonance-induced method necessitates alignment between the circularly polarized laser's polarization direction and the valley electron's Berry curvature.

Studies on ultrastrong terahertz sources [10] and single-cycle lasers with circular polarization [11] for valley manipulation have also been reported. Resonant excitation can achieve a high valley polarization rate, yet the subsequently published nonresonant schemes exhibit a faster operational rate. Jiménez-Galán et al. demonstrated the manipulation of valley polarization in band-gapped graphene [12], graphene [13], and bulk MoS_2 [14] using a cloverleaf laser with 2-color circular polarization pulses in a nonresonant manner. Additionally, numerical calculations [15–17] revealed that when the driving pulse is reduced to nearly a single cycle, a marked vector potential emerges at the peak instant of the laser, consequently inducing valley polarization. The necessity for a sufficiently large vector potential implies that the pulse possesses both an intense peak power and an extremely short duration. The above optical strategies demand meticulous pulse waveform design, extremely short pulses, and remarkably high peak intensities. Undoubtedly, these prerequisites present substantial challenges in the experimental realization and practical implementation of ultrafast valleytronic devices.

The pivotal importance of electron interference has been effectively unveiled in the phenomena of high-order harmonic generation [18–21] and strong-field ionization [22–25]. The application of quantum interference control via multiphoton processes [26–31] is increasingly recognized for its ability to facilitate the current injection in semiconductors. Encouragingly, previous studies [32,33] found that the strong-field resonance stemmed from the interference patterns of electrons occurring within and between optical cycles. Differing from the scenario in traditional electronic devices, quantum interference assumes a paramount role in laser-induced ultrafast dynamics for valleytronic devices. Based on the background, we present innovative insights into the pivotal role of quantum interference between the 1- and 2-photon transition pathways in valley polarization. Our results break the traditional view that photo-induced valley polarization requires only 2 co-linearly polarized beams, rather than 2 cross-linearly polarized beams that either form a circularly polarized light [6,7] or are time-separated

[8,9]. The achievement of femtosecond-level precision in valley manipulation marks a theoretical breakthrough, distinct from the traditional circularly polarized method. The importance of our work is twofold. On a theoretical level, we reveal the effectiveness of resonance laser-induced quantum path interference on valley polarization, which remains effective even when the laser width is compressed to nearly one cycle. On a practical level, this interference scheme can control the valley polarization in a few femtoseconds without necessitating excessively intense lasers. It is crucial for repetitive operations in valley devices at petahertz clock rates without causing material damage. Hence, the enduring challenge in valley ultrafast control—whether reaching petahertz operation rates or meeting rigorous laser parameters—is on the brink of being surmounted.

Methods

Perturbation model

A perturbation model for photocurrent injection in semiconductors is helpful for a quantitative description of our work. According to the theoretical research on 2-color-coherent current control in semiconductors [28], when considering the perturbative approximation and the complex amplitude of the linearly polarized laser $F = F_\omega e^{-i\omega t} + F_{2\omega} e^{-i(2\omega t+\varphi)}$, the induced carrier density takes the following form:

$$D(k) = \frac{v_{vc}v_{cv}}{\varepsilon_{cv}^2}F_{2\omega}^2 + 16\sum_{n,m}\frac{v_{vn}v_{nc}v_{cm}v_{mv}}{\left(\overline{\varepsilon}_{cv}-\varepsilon_n\right)\left(\overline{\varepsilon}_{cv}-\varepsilon_m\right)\varepsilon_{cv}^4}F_\omega^4 + 8\sum_n\frac{v_{vn}v_{nc}v_{cv}}{\left(\overline{\varepsilon}_{cv}-\varepsilon_n\right)\varepsilon_{cv}^3}F_{2\omega}F_\omega^2\sin(\varphi), \quad (1)$$

where v_{nm} are velocity operator matrix elements, whose lower corner notations represent valence (v) and conduction (c) bands, respectively. ε_n are energy bands, $\varepsilon_{cv} = \varepsilon_c - \varepsilon_v = 2\omega$, $\overline{\varepsilon}_{cv} = \left(\varepsilon_c + \varepsilon_v\right)/2$. Atomic units (a.u.) are used throughout the text unless otherwise stated. The first term of Eq. 1 represents 1-photon excitation, the second represents 2-photon excitation, and the third is an interference term between them. It is the time-reversal symmetry that causes the first 2 terms to be even functions of k, while the interference term is odd because it contains a k in the intraband velocity matrix elements [27,29]. Consequently, this leads to an asymmetric distribution of carriers within the Brillouin Zone (BZ). The theoretical model has been effectively employed in investigating photocurrent injection [26–31] in semiconductors.

Here, we extend this model to valley polarization and validate its applicability in monolayer hexagonal boron nitride (hBN) under the conditions of ultrafast lasers. Figure 1 shows a schematic diagram depicting valley polarization using a 2-color field. The electron density at the K/K' points excited by the 2-color field is denoted as $D_K/D_{K'}$. Then, the valley asymmetry is defined as

$$P = \frac{D_K - D_{K'}}{D_K + D_{K'}}. \quad (2)$$

By bringing Eq. 1 into the above formula and considering the dependence of each term in Eq. 1 on k, we get

$$\begin{cases} P = \dfrac{2}{\delta + 1/\delta}\sin(\varphi), \\ \delta = \dfrac{\varepsilon_{cv}^2 F_{2\omega}}{8\left(v_{vv} - v_{cc}\right)F_\omega^2}. \end{cases} \quad (3)$$

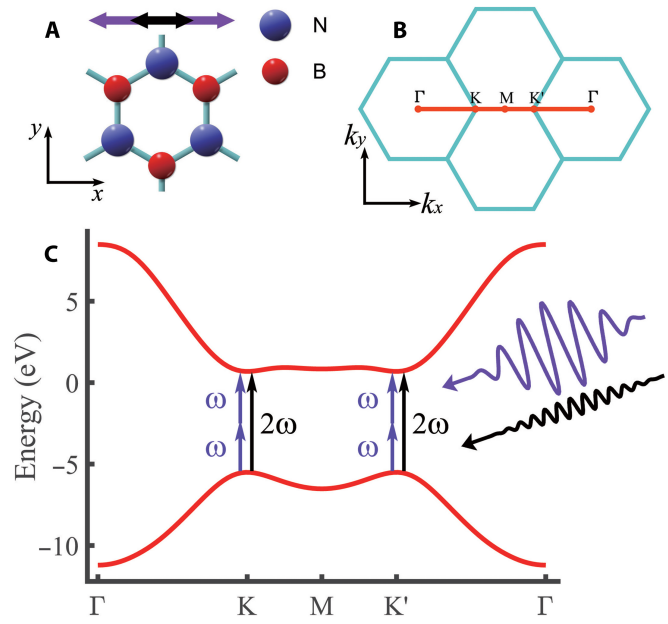

Fig. 1. Schematic diagram of valley polarization induced by a resonant 2-color field. The illustration above in (A) shows the structure of monolayer hBN in real space. Both the fundamental and double-frequency components (purple and black arrows) of the laser are polarized along the x-axis, i.e., the zigzag direction in real space. The reciprocal lattice is displayed in (B). The red curves in (C) are the cross-sections of the lowest conduction band and the highest valence band of hBN. The cross-section of the bands in reciprocal space is marked with a red line in (B). We translate the Γ point to the edge of the image solely for the convenience of presentation.

The valley asymmetry reaches the maximum $P = 1$ when $\varphi = \pi/2$ and $\delta = 1$, which requires $F_{2\omega} = 8F_\omega^2\left(v_{vv} - v_{cc}\right)/\varepsilon_{cv}^2$. Equation 3 delineates a quantitative relationship between the parameters of the material, the laser, and the induced electron asymmetry. When the 2-photon energy of the laser matches the minimum bandgap (i.e., $2\omega = \varepsilon_{cv,K}$), Eq. 3 indicates the asymmetry of the population at the points K/K', that is, the valley asymmetry.

Unlike the case at the Γ point, the third-order differential is nonzero at these points K/K', and the 2-photon process is not prohibited. A substitution value of $v_{vv} - v_{cc}$ can be derived in the following numerical calculations, thus making the model applicable for the material.

In general, the perturbative model assumes that the driving laser is weak and the depletion of electrons is negligible. Besides, the perturbative model is time-averaged and assumes that the field vector is sinusoidal. We attempt to use this model to compare with numerical simulation results to reveal the dynamical mechanism of valley polarization in our scheme. Therefore, the results are expected to be close to the model when using a relatively weak multicycle laser. However, due to the short lifetime of valley polarization and the requirement of operational rate, ultrafast laser-induced valley polarization is emphatically discussed in this paper.

Numerical method

In order to reveal the quantum interference mechanism in valley polarization, we use the method introduced in Refs. [34,35] to simulate the dynamics of the interaction between lasers and the material. In the semiconductor Bloch equations (SBEs), Bloch-like basis constructed by maximally localized Wannier

functions is employed. The method addresses the issues of discontinuous transition dipole moment phases [36] and the indispensable Berry connections [37], offering high precision and efficiency for simulating ultrafast dynamics in semiconductors. It has gained widespread recognition in the community.

Based on independent electron approximation and dipole approximation, the SBEs in Wannier gauge can be obtained from the time-dependent Schrödinger equation. The electron structure information of monolayer hBN is obtained by the Vienna ab initio simulation package (VASP) [38]. We adopt the local density approximation (LDA) in the exchange-correlation functional and use a $10 \times 10 \times 1$ grid in the KPOINTS file. The sampling points of k-space and real space, the cutoff energy of the plane-wave basis and the convergence criterion are verified to converge. Following the same treatment as in Ref. [34], we perform a projection on the p_z orbitals and get the matrix elements of Hamiltonian $\boldsymbol{H}_{nm}^{(W)}$ and transition dipole moment $\boldsymbol{D}_{nm}^{(W)}$ using the WANNIER90 package [39]. The superscript (W) refers to the Wannier gauge, and the subscripts are the band indices. The energy bands are well fitted over a broad range in the Wannier basis. The 2 energy bands corresponding to the projected orbitals, namely, the highest valence band and the lowest conduction band as shown in Fig. 1, are the bands involved in the SBEs.

The electron population at the end of the pulses can be obtained through the numerical solution of the SBEs in the form of density matrix [34,35]

$$\begin{aligned}&\frac{\partial \rho_{nm}^{(W)\boldsymbol{k}_0}(t)}{\partial t} = \\ &i\sum_l \left[H_{ln}^{(W)\boldsymbol{k}(t)}\rho_{lm}^{(W)\boldsymbol{k}_0}(t) - H_{ml}^{(W)\boldsymbol{k}(t)}\rho_{nl}^{(W)\boldsymbol{k}_0}(t)\right] \\ &+ i\boldsymbol{F}(t)\cdot\sum\left[\boldsymbol{D}_{ln}^{(W)\boldsymbol{k}(t)}\rho_{lm}^{(W)\boldsymbol{k}_0}(t) - \boldsymbol{D}_{ml}^{(W)\boldsymbol{k}(t)}\rho_{nl}^{(W)\boldsymbol{k}_0}(t)\right].\end{aligned} \tag{4}$$

$\boldsymbol{k}(t) = \boldsymbol{k}_0 + \boldsymbol{A}(t)$, where $\boldsymbol{k}_0$ is the initial crystal momentum and $\boldsymbol{A}(t)$ is the vector potential of laser field $\boldsymbol{F}(t)$. Inspired by these works [35,40], we use the time-dependent crystal momentum to eliminate the gradient term of k, thereby improving computational efficiency. At the initial moment of time evolution, all electrons at each k-point are populated in the valence band, and these electrons evolve independently. We employ an improved Euler method for time evolution, ensuring a time step $\leq$0.1 a.u. to guarantee convergence.

When considering the dephasing time T_2, the density matrix is converted to the Hamiltonian gauge at each step of the evolution. The dephasing term can be handled in the Hamiltonian gauge. Experiments (e.g., [41]) show that valley coherence persists for approximately 100 fs, but some numerical computation studies tend to use a much shorter dephasing time. Because we use a short wavelength (the optical cycle $T = 1.3$ fs) and ultrashort pulses, the calculations show few changes even when a short dephasing time (e.g., $T_2 = 5$ fs) is used. Therefore, the dephasing time has a minor impact on the few-cycle dynamics driven by short-wavelength lasers, and we ignored it in our calculations except where specified in the following text.

Results and Discussion

In the numerical simulations, the driving laser takes the following form:

$$\boldsymbol{F}(t) = f(t)\left[F_\omega \cos\left(\omega t + \varphi_{cep}\right) + F_{2\omega}\cos\left(2\omega t + 2\varphi_{cep} + \varphi\right)\right]\hat{x}, \tag{5}$$

where

$$f(t) = \begin{cases} \cos^2(\pi t/\tau) & -\tau/2 < t < \tau/2, \\ 0 & else, \end{cases}$$

is an envelope with a total duration of τ, and the full width at half maximum (FWHM) is labeled as $\sigma \approx 0.364\,\tau$. φ_{cep} is the carrier-envelope phase (CEP), and φ is a relative phase between the 2 pulses.

We fix $\varphi = \pi/2$ and $\omega = \varepsilon_{cv,K}/2 = 0.114$ a.u., where $\varepsilon_{cv,K}$ is the minimum bandgap, and perform numerical calculations with varying laser peaks and duration. According to the definition in Eq. 2, once the conduction band populations at the K/K' points are obtained, the parameter-dependent valley asymmetry can be derived, as depicted in Fig. 2. For illustrative purposes, we define the abscissa as $\tilde{F}_{2\omega} = \varepsilon_{cv}^2 F_{2\omega}/\left(8F_\omega^2\right)$. In Fig. 2A, we use multi-cycle pulses with $\tau = 80\,T$ (where $T = 2\pi/\omega$) corresponding to $\sigma = 39$ fs, and $\varphi_{cep} = 0$. When $F_\omega < 0.002$ a.u. (corresponding to the intensity $I = 0.14$ TW/cm^2), the data converge to a curve and have a maximum at $\tilde{F}_{2\omega} = 0.05$ a.u. We substitute this value for $v_{vv} - v_{cc}$ in Eq. 3 and express this equation with green dots in Fig. 2. These points perfectly coincide with the curves converged by numerical calculations. When $F_\omega \geq 0.02$ a.u., the results of SBEs deviate from the perturbation model. In Fig. 2B and C, we fix $F_\omega = 0.001$ a.u. and adopt few-cycle pulses. We find that when the FWHM approaches 1 fs (which is less than one cycle), the curves show a tendency to deviate from the perturbative model and exhibit CEP dependence. We varied the CEP within a range $\varphi_{cep} \in [-\pi, \pi]$ and find that when $\varphi_{cep} = \pm\pi/2$, the fluctuation range of the curves reaches maximum. As can be seen, when there is no the second harmonic laser ($\tilde{F}_{2\omega} = 0$), there is an inherent valley asymmetry that varies with the CEP. This is due to the inherent asymmetry of the pulses, and similar phenomena are discussed in these literatures [15,16]. Our results demonstrate the precision of quantifying valley polarization using the perturbation model, but the quantum path interference is not confined to the scope of perturbative approximation. We vary the laser parameters widely in our calculations, ranging from a power density of 10^8 W/cm^2 to 10^{13} W/cm^2 and a pulse duration from a few femtoseconds to hundreds of femtoseconds, and the maximum valley asymmetry consistently approaches nearly 100%. Even in extreme cases where the laser is ultrastrong or ultrashort, the numerical results deviate from the perturbative model, but the maximum value of valley asymmetry consistently maintains good robustness. These results are favorable for experimental implementation because, once the relative phase and intensity of the 2 beams are determined, excessively intense lasers and CEP locking are unnecessary. The model and numerical results successfully demonstrate the effectiveness of the quantum interference control for valley polarization. The results show that the quantum path interference scheme can polarize valley in a time close to 1 fs while reducing the requirement for laser intensity, which is a breakthrough for the ultrafast control of valley.

Within the parameters of our interest, the short resonant wavelength and a large bandgap of hBN offer a Keldysh parameter [42]

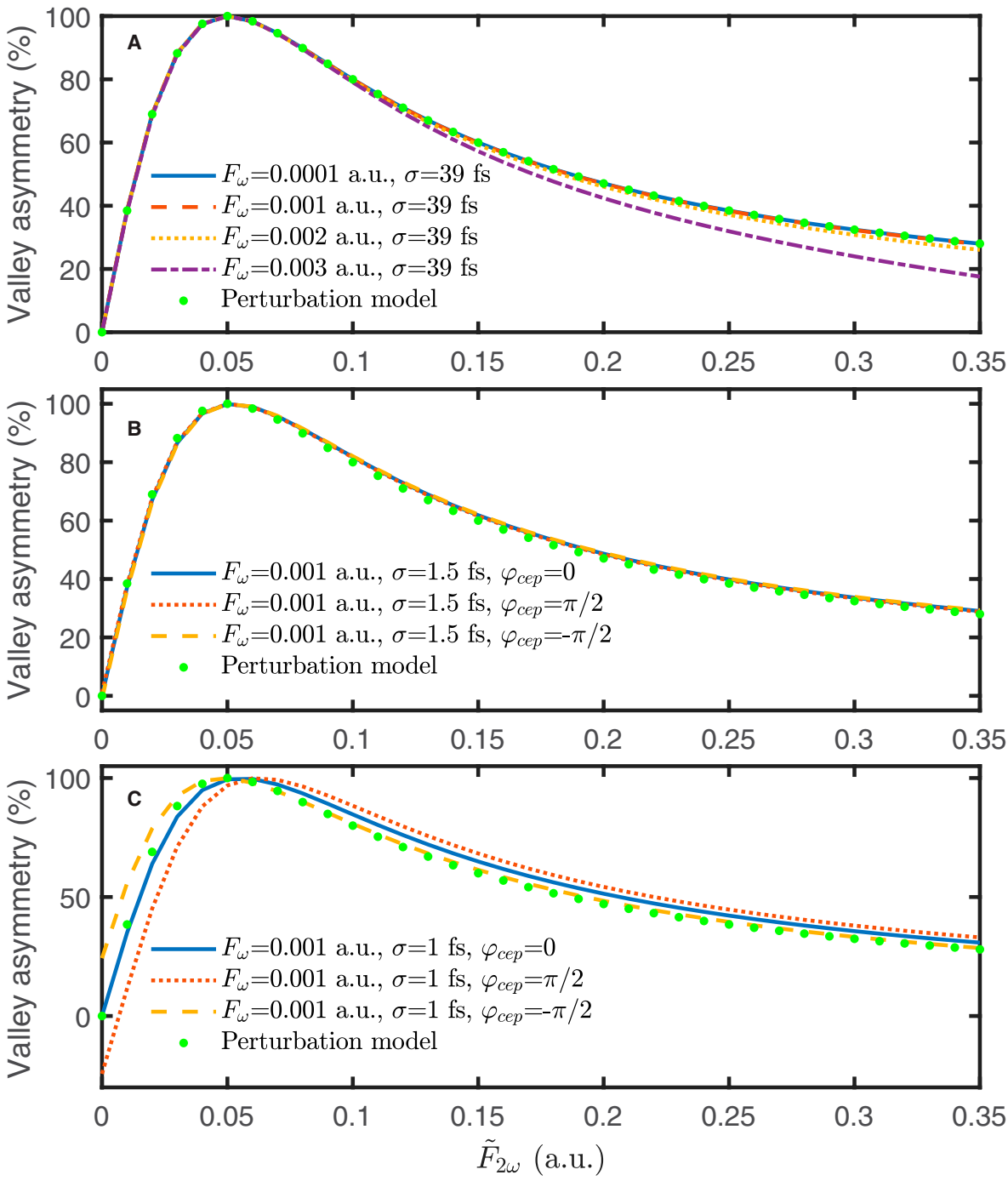

Fig. 2. Valley asymmetry P as a function of laser peaks and FWHM. The curves depict the results of numerical calculations, in which F_ω and σ are illustrated in the legend, $\varphi = 0.5\pi$, and $\omega = 0.114$ a.u. The green dots represent the results of the perturbation model. Multi-cycle pulses are used in (A), and few-cycle pulses are used in (B) and (C).

that is markedly greater than 1, providing an excellent prerequisite for the resonant scheme. As emphasized in previous studies [32,33], driven by ultrafast lasers, resonance manifests as coherent interference between excitation pathways in adjacent cycles. When the phase difference between the excitation pathways is $2\pi q$, where q corresponds to the number of photons, the population of conduction band rises rapidly within subcycles. The temporal resolution of the 2ω light is twice that of the fundamental frequency light. This allows for precise shaping of the waveform within one optical cycle and breaks symmetry of the laser. Consequently, manipulation of interference in subcycles occurs, resulting in constructive interference at K and destructive interference at K'. Although the laser's duration is too short or its intensity is too strong, deviating markedly from the approximation of the perturbation model, as long as a complete interference can be ensured within the pulse, a high degree of valley asymmetry can be achieved. Therefore, the large Keldysh parameter and the interference dynamics within few cycles together ensure the effectiveness of our scheme under ultrafast laser excitation. This is also why, when the laser is almost beyond the general perturbation region, the numerical calculations still show a good agreement with the perturbation model.

The curves in Fig. 3 show φ-dependent valley asymmetry obtained by the numerical calculations, and the green dots represent Eq. 3 with $\delta = 1$. The numerical calculations are consistent with the perturbation model and illustrate the characteristic phase dependence inherent in quantum interference. The phases $\varphi = 0.5\pi$, π, and 1.5π encoded in the ultrafast laser correspond to the induced valley pseudospin $+1$, 0, -1, respectively. This phase of the laser directly influences the phase of the quantum paths, thus enabling the subcycle dynamics of valley polarization to be effectively controlled through a single and controllable laser parameter. The decrease in asymmetry is anticipated when it is integrated near the K/K' points, as the selected laser parameters are specifically optimized for the polarization of the K/K' points only. The purpose of integration is to include more electrons that have the potential to contribute to the valleys, which is a common practice in the published calculations. The potential contributions mainly come from the scattering-induced electron diffusion in k-space. Electron–electron scattering and electron–phonon scattering, while having a minor effect on few-cycle dynamics, may alter the lattice momentum of electrons during the observation period. Thus, efforts to optimize the integrated valley asymmetry should be approached from 2 directions. One is to enhance the targeting of polarization to avoid the excitation of nonpolarized and nonvalley electrons. The other is to reduce the impact of scattering by improving the observation technique.

Figure 4 illustrates the k-resolved electron occupations in the conduction band at the end of driving lasers, with $\varphi = 0.5\pi$ in Fig. 4A and C, and $\varphi = 1.5\pi$ in Fig. 4B and D. In the hexagonal BZ, one can see that the electron distribution is extremely asymmetric, primarily concentrated at the K/K' points. The outcomes underscore 2 advantages of resonant excitation over nonresonant excitation for valley polarization: it enables targeted excitation of K/K' points and obviates the need for excessively strong or excessively short lasers. Studies [6,43] indicate that the valley selection rule holds true near the K/K' points, implying that electrons located away from these points do not exhibit valley characteristics. Consequently, exciting electrons distant from the

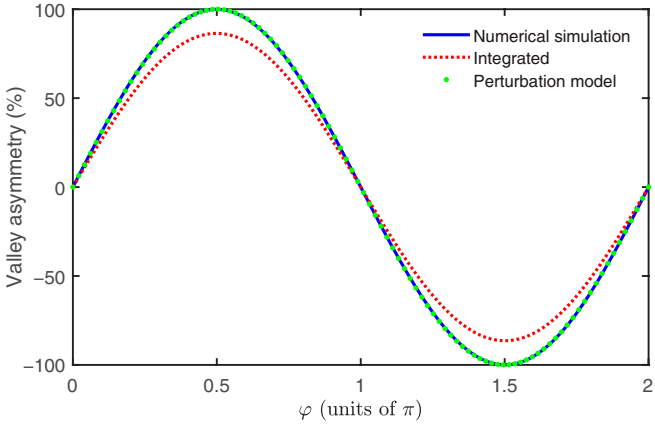

Fig. 3. Valley asymmetry P as a function of the relative phase φ. The blue solid and red dashed curves represent the numerical results. The electron density at K/K' points is replaced by that integrated near K/K' points for the red dashed curve, and the integral covers an area within a circle with a radius of 0.04 a.u. The green dots depict the results of the perturbation model. Here, $F_\omega = 2.0 \times 10^{-3}$ a.u., $F_{2\omega} = 3.0 \times 10^{-5}$ a.u., and $\sigma = 9.7$ fs; other parameters are the same as those in Fig. 2.

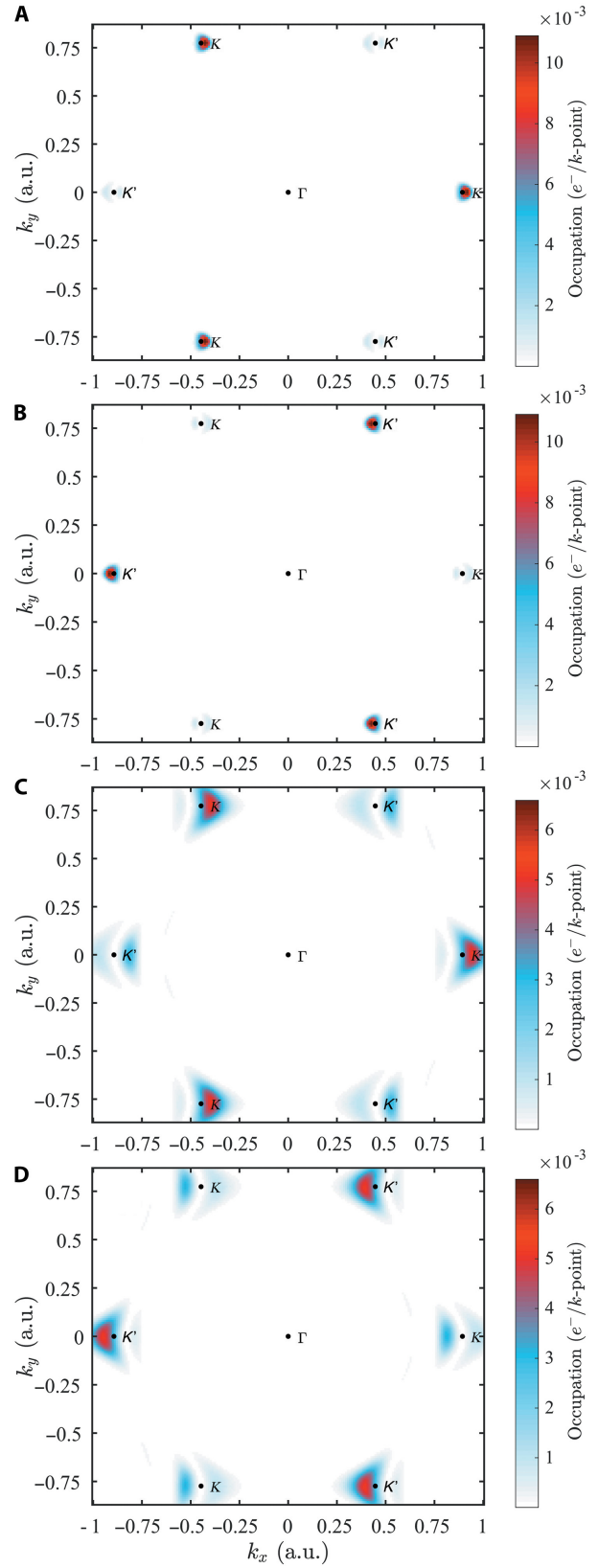

Fig. 4. k-resolved electron occupations in the conduction band after the 2-color lasers. A multi-cycle pulse is used in (A) and (B) with the same parameters as that in Fig. 3, and $\varphi = 0.5\pi$ and 1.5π, respectively. (C) and (D) are similar to (A) and (B), but a few-cycle pulse is used with $\sigma = 2.9$fs, $F_\omega = 4.0 \times 10^{-3}$a.u., and $F_{2\omega} = 1.2 \times 10^{-4}$a.u.; other parameters are the same as those before. High-symmetry points are marked with black dots.

K/K' points offer no advantage, particularly considering the potential material damage caused by excessive electron excitation. The lasers have an FWHM of 20 fs in Fig. 4A and B, and 2.9 fs in Fig. 4C and D, respectively. For the 2 lasers, the integrated valley asymmetry achieves 85% and 83%, respectively. When the laser is compressed to few femtoseconds, the selective excitation still obtains a high valley asymmetry, even if the electron distribution becomes somewhat dispersed. The polarization degree of electrons away from the valleys is slightly lower, thus reducing the integrated valley asymmetry. This result suggests that, within the operational rate limits, using lasers with better monochromaticity can enhance the integrated valley asymmetry. In addition, with the advancement of detection schemes, valley polarization can be rapidly read out within the valley coherence time, thus reducing the diffusion caused by scattering, which will also improve the measured valley asymmetry.

Apart from the valley asymmetry described in Eq. 2, the absolute occupation difference between K/K' valleys has practical importance for experimental observations. According to the perturbation model, $\left(D_K - D_{K'}\right) \propto F_{2\omega} F_\omega^2 / \varepsilon_{cv}^4$ (the third term in Eq. 1), and considering the condition for maximum valley polarization $F_{2\omega} = 8F_\omega^2 \left(v_{vv} - v_{cc}\right)/\varepsilon_{cv}^2$ in Eq. 3, we get the absolute occupation difference

$$\left(D_K - D_{K'}\right) \propto \frac{F_\omega^4}{\varepsilon_{cv}^6}. \tag{6}$$

We can see in Fig. 4A that the absolute occupation difference at K/K' exceeds 0.01 e^-/k-point. Comparing this to the situation in experiments, this absolute occupancy difference is considered observable with existing experimental means. Since the hBN has a large bandgap of 6.2 eV in our calculations, when using an ultrashort pulse, the number of polarized valley electrons ($\propto \varepsilon_{cv}^{-6}$) is relatively small. This implies that the material has a high damage threshold. In the experiment in Ref. [5], the damage threshold for hBN is bigger than 7 TW/cm^2 for 2-μm and 1-μm counter-rotating lasers with durations of 26 and 48 fs. Although a short wavelength is adopted in our study, the intensity ($F_\omega = 0.002$ a.u. corresponds to $I = 0.14$ TW/cm^2) and pulse width (few femtoseconds) are much smaller than those in the experiment. Therefore, there is a marked safety margin for the laser we use in terms of the damage threshold. On the other hand, thanks to the high efficiency of resonant excitation ($\propto F_\omega^4$), the absolute occupation difference is rapidly increased when appropriately increasing the laser intensity or using a material with a smaller bandgap. Nevertheless, in contrast to the nonresonant schemes, there is no extreme requirement for laser intensity. The successful application of valley devices will be accompanied by the progress of valley reading technology, and the requirements for laser intensity will be further reduced.

We try to demonstrate the ultrafast writing, erasing, and rewriting of valley driven by a pulse sequence based on the scheme of quantum path interference. The simulation results are shown in Fig. 5. The 3 pulses share the same parameters except for the relative phase φ and the order of appearance. After each pulse, the conduction band electron occupations at K/K' points are extracted to obtain the absolute occupation difference, which is displayed as scatter points in the figure. We can see that after the action of the first pulse within a few

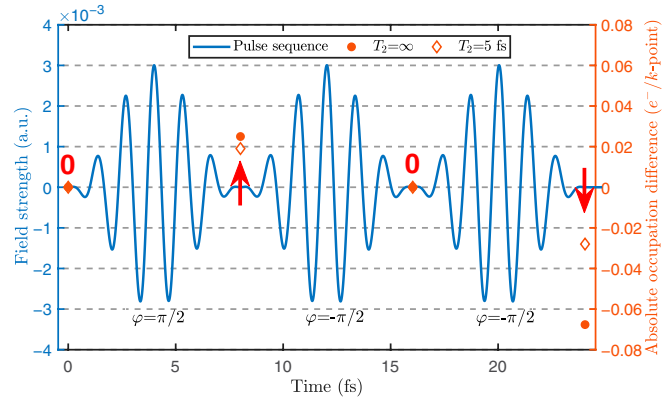

Fig. 5. An example of manipulating valley polarization with ultrafast pulse trains. The blue curve represents the field strength of a pulse sequence composed of 2-color linearly polarized pulses. The first pulse with $\varphi = \pi/2$, and the following two with $\varphi = -\pi/2$. The pulses share the same parameters except for the relative phase and the order of appearance. $\tau = 6T$, $F_\omega = 3.0 \times 10^{-3}$ a.u., $F_{2\omega} = 7.0 \times 10^{-5}$ a.u., and $\varphi_{cep} = 0$. The red circular and diamond scatter points represent the absolute occupation differences caused by these pulses, with dephasing times of infinity and 5 fs, respectively. The red arrows indicate the direction of the valley pseudospin after each pulse.

femtoseconds, the valley is polarized, which can be considered as the pseudospin pointing upwards, represented by a red arrow. Following the second pulse, the valley polarization is erased. Subsequently, the third pulse induces an opposite pseudospin. The operating switch time in few femtoseconds implies a writing rate in petahertz. When employing even shorter pulses, this operating rate can be further increased. As we anticipated, thanks to the extremely short pulse width, the dephasing time has little impact on the valley polarization within a pulse. The calculations in Refs. [8,9] showed that valley polarization oscillates and decays with the increase of the delay between pulses, because the mechanism in those papers depends on the coherence between pulses. However, this is not the case here. We change the delay between the pulses, and the valley asymmetry remains almost unchanged. This is because the interference of these 2 quantum paths (the 2 excitation channels ω and 2ω) relies on coherence only within pulse. Therefore, in practical operation, once the relative phase is locked, fluctuations in the time delay between pulses do not affect the results. The absolute occupation difference after the third pulse is greater than that after the first pulse, which is due to the coherence between pulses. Because the coherence and accumulation effects between pulses are more markedly affected by the dephasing time, when a short dephasing time is used, the absolute occupation difference after the third pulse is markedly suppressed. Despite this, coherence is well maintained within each pulse, ensuring that the effectiveness of the subsequent pulses is not diminished. Furthermore, following the practice in the paper [17], the results after each pulse can be improved by adjusting the individual intensities of the pulses. The weak dependence on dephasing time, pulse delay, and CEP mentioned above are undoubtedly beneficial for experimental implementation.

Conclusion

In conclusion, we reveal the pivotal role of quantum interference based on 1- and 2-photon resonance in the dynamics of valley polarization, providing the first evidence that resonant

valley polarization does not necessitate the involvement of circularly polarized or cross-linearly polarized lasers.

The mechanism of valley polarization achieves a breakthrough in femtosecond resolution due to the interference dynamics and the shorter wavelength. Hence, the resonant 2-color pulses can induce higher valley asymmetry at a faster rate without the need to compress the laser into a single cycle.

More crucially, complex circularly polarized or exceedingly intense lasers are unnecessary, greatly reducing the implementation difficulty for all-optical ultrafast valley control. Additionally, the valley polarization can be switched easily via a unique phase of the lasers. The generation of photons with detectable polarization properties from polarized valley states, accomplished within an ultrafast timeframe, signifies the capability for ultrafast manipulation of photonic states. We demonstrate the feasibility of information transfer between photon energy, photon spin angular momentum, and valleys at petahertz clock rates. This research holds immense promise as the cornerstone for a new generation of storage and operational components reliant on ultrafast valley control.

Acknowledgments

We sincerely thank Dr. H.-C. Du, J.-X. Chen, and T.-J. Shao for their assistance in the numerical method, as well as the helpful discussions with Professor T. T. Luu.

Funding: This work was supported by the Hubei Provincial Natural Science Foundation of China (Grant No. 2024AFA029), the National Natural Science Foundation of China (Grant No. 12204492), and the CAS Project for Young Scientists in Basic Research (Grant No. YSBR-059).

Author contributions: L-J.L. built the model and executed the calculations. Both authors contributed to the discussion of the data and the writing of the manuscript. X.-B.B. supervised this project as a whole.

Competing interests: The authors declare that they have no competing interests.

Data Availability

The data that support the plots within this paper are available from the corresponding author upon reasonable request.

References

1. Goulielmakis E, Yakovlev VS, Cavalieri AL, Uiberacker M, Pervak V, Apolonski A, Kienberger R, Kleineberg U, Krausz F. Attosecond control and measurement: Lightwave electronics. *Science*. 2007;317(5839):769–775.
2. Krausz F, Stockman MI. Attosecond metrology: From electron capture to future signal processing. *Nat Photonics*. 2014;8:205–213.
3. Ludwig M, Aguirregabiria G, Ritzkowsky F, Rybka T, Marinica DC, Aizpurua J, Borisov AG, Leitenstorfer A, Brida D. Sub-femtosecond electron transport in a nanoscale gap. *Nat Phys*. 2020;16:341–345.
4. Vitale SA, Nezich D, Varghese JO, Kim P, Gedik N, Jarillo-Herrero P, Xiao D, Rothschild M. Valleytronics: Opportunities, challenges, and paths forward. *Small*. 2018;14(38):Article e1801483.
5. Mitra S, Jiménez-Galán Á, Aulich M, Neuhaus M, Silva REF, Pervak V, Kling MF, Biswas S. Light-wave-controlled Haldane model in monolayer hexagonal boron nitride. *Nature*. 2024;628(8009):752–757.
6. Zeng H, Dai J, Yao W, Xiao D, Cui X. Valley polarization in MoS_2 monolayers by optical pumping. *Nat Nanotechnol*. 2012;7(8):490–493.
7. Mak KF, He K, Shan J, Heinz TF. Control of valley polarization in monolayer MoS_2 by optical helicity. *Nat Nanotechnol*. 2012;7:494–498.
8. Sharma S, Elliott P, Shallcross S. Valley control by linearly polarized laser pulses: Example of WSe_2. *Optica*. 2022;9(8):947–952.
9. Silva REF, Ivanov M, Jiménez-Galán Á. All-optical valley switch and clock of electronic dephasing. *Opt Express*. 2022;30(17):30347–30355.
10. Langer F, Schmid CP, Schlauderer S, Gmitra M, Fabian J, Nagler P, Schüller C, Korn T, Hawkins PG, Steiner JT, et al. Lightwave valleytronics in a monolayer of tungsten diselenide. *Nature*. 2018;557:76–80.
11. Oliaei Motlagh SA, Wu J-S, Apalkov V, Stockman MI. Femtosecond valley polarization and topological resonances in transition metal dichalcogenides. *Phys Rev B*. 2018;98(8):081406.
12. Jiménez-Galán Á, Silva REF, Smirnova O, Ivanov M. Lightwave control of topological properties in 2D materials for sub-cycle and non-resonant valley manipulation. *Nat Photonics*. 2020;14:728–732.
13. Mrudul MS, Jiménez-Galán Á, Ivanov M, Dixit G. Light-induced valleytronics in pristine graphene. *Optica*. 2021;8(3):422–427.
14. Tyulnev I, Jiménez-Galán Á, Poborska J, Vamos L, Russell PSJ, Tani F, Smirnova O, Ivanov M, Silva REF, Biegert J. Valleytronics in bulk MoS_2 with a topologic optical field. *Nature*. 2024;628(8009):746–751.
15. Jiménez-Galán Á, Silva REF, Smirnova O, Ivanov M. Sub-cycle valleytronics: Control of valley polarization using few-cycle linearly polarized pulses. *Optica*. 2021;8(3):277–280.
16. Hashmi A, Yamada S, Yamada A, Yabana K, Otobe T. Valley polarization control in WSe_2 monolayer by a single-cycle laser pulse. *Phys Rev B*. 2022;105:Article 115403.
17. Rana N, Dixit G. All-optical ultrafast valley switching in two-dimensional materials. *Phys Rev Appl*. 2023;19(3):Article 034056.
18. Lein M, Hay N, Velotta R, Marangos JP, Knight PL. Role of the intramolecular phase in high-harmonic generation. *Phys Rev Lett*. 2002;88(18):Article 183903.
19. McFarland BK, Farrell JP, Bucksbaum PH, Gühr M. High harmonic generation from multiple orbitals in N_2. *Science*. 2008;322(5905):1232–1235.
20. Wörner HJ, Niikura H, Bertrand JB, Corkum PB, Villeneuve DM. Observation of electronic structure minima in high-harmonic generation. *Phys Rev Lett*. 2009;102(10):Article 103901.
21. Luu TT, Yin Z, Jain A, Gaumnitz T, Pertot Y, Ma J, Wörner HJ. Extreme-ultraviolet high-harmonic generation in liquids. *Nat Commun*. 2018;9(1):3723.
22. Yurchenko SN, Patchkovskii S, Litvinyuk IV, Corkum PB, Yudin GL. Laser-induced interference, focusing, and diffraction of rescattering molecular photoelectrons. *Phys Rev Lett*. 2004;93(22):Article 223003.
23. Klaiber M, Hatsagortsyan KZ, Keitel CH. Tunneling dynamics in multiphoton ionization and attoclock calibration. *Phys Rev Lett*. 2015;114(8):Article 083001.

24. Serebryannikov EE, Zheltikov AM. Strong-field photoionization as excited-state tunneling. *Phys Rev Lett*. 2016;116(12):Article 123901.
25. Liu M, Xu S, Hu S, Becker W, Quan W, Liu X, Chen J. Electron dynamics in laser-driven atoms near the continuum threshold. *Optica*. 2021;8(6):765, 770.
26. Kurizki G, Shapiro M, Brumer P. Phase-coherent control of photocurrent directionality in semiconductors. *Phys Rev B*. 1989;39(5):3435–3437.
27. Atanasov R, Haché A, Hughes JLP, van Driel HM, Sipe JE. Coherent control of photocurrent generation in bulk semiconductors. *Phys Rev Lett*. 1996;76(10):1703–1706.
28. van Driel HM, Sipe JE. Chapter 5. Coherence control of photocurrents in semiconductors. In: Tsen K-T, editor. *Ultrafast phenomena in semiconductors*. Berlin (Germany): Springer-Verlag; 2000. p. 261–306.
29. Fortier TM, Roos PA, Jones DJ, Cundiff ST, Bhat RDR, Sipe JE. Carrier-envelope phase-controlled quantum interference of injected photocurrents in semiconductors. *Phys Rev Lett*. 2004;92(14):Article 147403.
30. Rioux J, Sipe JE. Optical injection processes in semiconductors. *Phys E Low Dimens Syst Nanostructures*. 2012;45:1–15.
31. Wang K, Muniz RA, Sipe JE, Cundiff ST. Quantum interference control of photocurrents in semiconductors by nonlinear optical absorption processes. *Phys Rev Lett*. 2019;123(6):067402.
32. Wismer MS, Kruchinin SY, Ciappina M, Stockman MI, Yakovlev VS. Strong-field resonant dynamics in semiconductors. *Phys Rev Lett*. 2016;116(19):Article 197401.
33. Lü L-J. Wavepacket-interference view of optical excitation. *J Phys B Atomic Mol Phys*. 2021;54:Article 085602.
34. Silva REF, Martín F, Ivanov M. High harmonic generation in crystals using maximally localized Wannier functions. *Phys Rev B*. 2019;100(19):Article 195201.
35. Zhang Y, Zhang M, Yang W, Yu H, Si MS, Xue S, Du H. Defects of the nearest-neighbor tight-binding model in the study of solid harmonics. *Phys Rev A*. 2023;108(4):Article 043508.
36. Jiang S, Wei H, Chen J, Yu C, Lu R, Lin CD. Effect of transition dipole phase on high-order-harmonic generation in solid materials. *Phys Rev A*. 2017;96(5):Article 053850.
37. Li J, Zhang X, Fu S, Feng Y, Hu B, Du H. Phase invariance of the semiconductor Bloch equations. *Phys Rev A*. 2019;100(4):Article 043404.
38. Kresse G, Furthmüller J. Efficient iterative schemes for ab initio total-energy calculations using a plane-wave basis set. *Phys Rev B*. 1996;54(16):11169–11186.
39. Mostofi AA, Yates JR, Lee Y-S, Souza I, Vanderbilt D, Marzari N. wannier90: A tool for obtaining maximally-localised Wannier functions. *Comput Phys Commun*. 2008;178(9):685–699.
40. Vampa G, McDonald CR, Orlando G, Klug DD, Corkum PB, Brabec T. Theoretical analysis of high-harmonic generation in solids. *Phys Rev Lett*. 2014;113(7):Article 073901.
41. Hao K, Moody G, Wu F, Dass CK, Xu L, Chen C-H, Sun L, Li M-Y, Li L-J, MacDonald AH, et al. Direct measurement of exciton valley coherence in monolayer WSe_2. *Nat Phys*. 2016;12:677.
42. Keldysh LV. Ionization in the field of a strong electromagnetic wave. *Sov Phys JETP*. 1964;20:1307–1314.
43. Xiao D, Liu G-B, Feng W, Xu X, Yao W. Coupled spin and valley physics in monolayers of MoS_2 and other group-VI dichalcogenides. *Phys Rev Lett*. 2012;108(19):Article 196802.